

Design and Control of a Compact Series Elastic Actuator Module for Robots in MRI Scanners

Binghan He, Naichen Zhao, David Y. Guo, Charles H. Paxson, and Ronald S. Fearing

Abstract—In this study, we introduce a novel MRI-compatible rotary series elastic actuator module utilizing velocity-sourced ultrasonic motors for force-controlled robots operating within MRI scanners. Unlike previous MRI-compatible SEA designs, our module incorporates a transmission force sensing series elastic actuator structure, with four off-the-shelf compression springs strategically placed between the gearbox housing and the motor housing. This design features a compact size, thus expanding possibilities for a wider range of MRI robotic applications. To achieve precise torque control, we develop a controller that incorporates a disturbance observer tailored for velocity-sourced motors. This controller enhances the robustness of torque control in our actuator module, even in the presence of varying external impedance, thereby augmenting its suitability for MRI-guided medical interventions. Experimental validation demonstrates the actuator’s torque control performance in both 3 Tesla MRI and non-MRI environments, achieving a settling time of 0.1 seconds and a steady-state error within 2% of its maximum output torque. Notably, our force controller exhibits consistent performance across low and high external impedance scenarios, in contrast to conventional controllers for velocity-sourced series elastic actuators, which struggle with steady-state performance under low external impedance conditions.

I. INTRODUCTION

While robots have proven effective in enhancing the precision and time efficiency of MRI-guided interventions across various medical applications [1], safety remains a formidable challenge for robots operating within MRI environments due to several factors. As the robots assume full control of medical procedures, the reliability of their operation becomes paramount. Precise control over robot forces is particularly crucial to ensure safe interaction within the MRI environment. Furthermore, the confined space in the MRI bore complicates the safe operation

This work was supported by the National Institutes of Health under Grant R01MH127104. The content is solely the responsibility of the authors and does not necessarily represent the official views of the National Institutes of Health. (*Corresponding author: Binghan He.*)

Binghan He, Naichen Zhao, and Ronald S. Fearing are with the Department of Electrical Engineering and Computer Sciences, University of California, Berkeley, CA 94720 USA (e-mail: binghan.he@berkeley.edu, nzhao11235@berkeley.edu, ronf@berkeley.edu).

David Y. Guo and Charles H. Paxson are with the Department of Mechanical Engineering, University of California, Berkeley, CA 94720 USA (e-mail: dguo001@berkeley.edu, chpaxson@berkeley.edu).

of human-robot interaction, presenting challenges to maneuverability. However, there exists a notable scarcity of force-controlled robot actuators specifically tailored for MRI applications.

Unlike non-MRI environments, the strong magnetic field within MRI scanners renders conventional electromagnetic robot actuators unsafe for medical applications in MRI. While fluidic actuators offer MRI compatibility [2], [3], the lack of back-drivability in hydraulic actuators poses significant risks in medical scenarios involving human interaction. Pneumatic actuators [4], known for their compliance, enhance safety in human-robot interactions, yet their restricted force output and controllability confine their applicability to specific medical procedures, such as needle-based interventions [5]. Hydrostatic transmissions, driven by remote electromagnetic motors, offer another solution for MRI-compatible actuation by transferring motor forces through extended hoses [6]. However, the high piston seal friction inherent in hydrostatic transmissions introduces additional uncertainty in force control precision.

Non-magnetic electric motors, such as electrostatic motors [7] and ultrasonic motors (USMs) [8], [9], have been developed to provide both precision and compatibility with MRI environments. However, electrostatic motors require an extremely high voltage source to generate significant output force and are not commercially available. Akin to hydraulic actuators, USMs encounter inherent challenges such as high impedance and lack of backdrivability. Typically, USMs are utilized as velocity sources, restricting their applications to controlling human-robot interaction forces.

In [10], the series elastic actuator (SEA) concept introduces a unique architecture for robot actuators, enhancing safety during human-robot interaction. By placing a spring element in series with a rigid actuator, compliance is added. While traditional SEAs use force-sourced motors, this approach also benefits velocity-sourced actuators [11]. The spring element functions as a force sensor via Hooke’s law, enabling the control of actuator force to be translated into the control of spring deflection.

The development of MRI-compatible SEAs is initially presented in [12] for the implementation of an MRI-guided rehabilitation robot. This system achieves force-controlled actuation by integrating an USM, a pair of extension springs serving as the spring element, and a

linear bearing. The evolution of this technology continued with a rotary SEA in [13]. However, this particular actuator relies on an electromagnetic motor located outside the MRI room, connected via a lengthy cable-driven transmission, thus limiting its applicability for in-bore MRI robotic tasks. Notably, while compact SEA designs based on electromagnetic motors have been extensively investigated in non-MRI robot applications [14], [15], [16], [17], the development of integrated compact SEAs utilizing MRI-compatible motors remains an area yet to be fully explored.

Achieving effective force control for velocity-sourced SEAs poses another significant challenge, especially in MRI applications. For the MRI-compatible SEAs in [12], [13], proportional (P) or proportional-integral (PI) controllers have been used for actuator force control. However, their performance and stability heavily depend on the external impedance affecting the actuator. In scenarios where MRI robot applications involve substantial variation in external impedance, the closed-loop system behavior becomes uncertain. To address this challenge, the disturbance observer (DOB) method [18] has been integrated into numerous SEA control applications. The DOB calculates the difference between the input of the actual SEA system and that of a reference model. This difference is then compensated to ensure that the adjusted system behavior matches the reference model. Since the parameters of the DOB are independent of external impedance variations, it enhances the robustness of force control. Although this approach has been studied for SEAs employing force-sourced or position-controlled motors [14], [15], [19], its application to velocity-sourced motors has not been thoroughly examined.

In this study, we aim to address the above-mentioned challenges associated with MRI-compatible force-controlled actuators for robotic applications within MRI scanners. Diverging from prior MRI-compatible SEAs developed for rehabilitation robots [12], [13], which consistently interact with human patients, the SEA in this study is motivated by MRI-guided brain stimulation applications illustrated in Fig. 1. This requires a compact design for in-bore actuation and robust force control to handle varying external impedance, ensuring the robot can safely control forces during the transition from free motion to contact. The primary contributions of this paper are summarized as follows.

- (1) In Sec. II, we introduce a compact MRI-compatible SEA module that seamlessly integrates an USM, a rotary gearbox, and a spring element into a transmission force sensing SEA structure, as depicted in Fig. 2(b). Notably, this SEA is the first rotary SEA to operate entirely within an MRI scanner.
- (2) In Sec. III we present a DOB-based controller for actuator torque control in our compact SEA module. Notably, our DOB-based controller is specifically crafted for SEA systems featuring velocity-sourced motors, such as the MRI-compatible velocity-

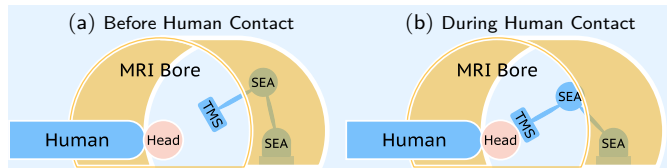


Fig. 1: Illustrated in (a) and (b), an SEA robot maneuvers a transcranial magnetic stimulator (TMS) towards a patient's head. The SEA force controller needs to address the challenges posed by both (a) the minimal external impedance of the medical device before it makes contact with the patient and (b) the substantial impedance encountered upon contact with the human body.

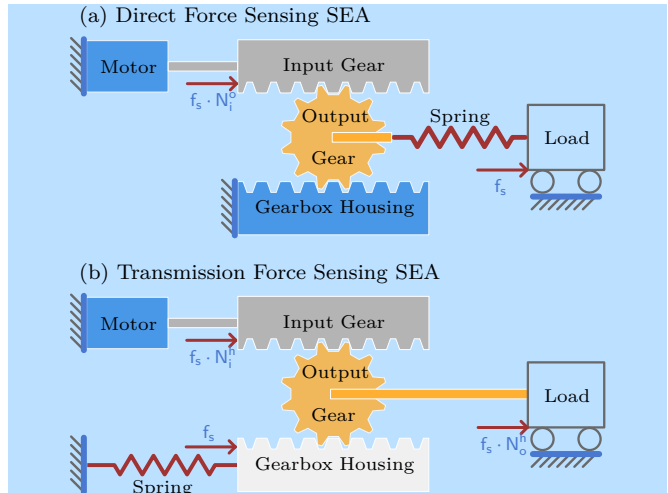


Fig. 2: In (a), a conventional direct force sensing SEA positions its spring element between the output gear and the load. Contrarily, in (b), a transmission force sensing SEA situates its spring element between the gearbox housing and the ground. The transmission force sensing SEA architecture enables the construction of a more compact SEA suitable for MRI scanners. f_s denotes the spring force. N_i^o , N_i^h , and N_o^h denote the gear ratios between the input and the output, between the input and the gearbox housing, and between the output and the gearbox housing.

controlled USM integrated into our SEA module.

- (3) In Sec. IV we demonstrate the consistent performance of our SEA module in both 3 Tesla MRI and non-MRI environments. In comparison to direct force control strategies employed in velocity-sourced SEAs [11], [12], [13], our DOB-based controller exhibits its capability to handle both low and high impedance loads.

II. MECHANICAL DESIGN

In this section, we present a compact SEA design that seamlessly integrates an USM, a rotary gearbox, and a spring element into a unified module. Towards the conclusion, we offer a comparative analysis with previous MRI-compatible SEAs and assess the MRI-compatibility of our SEA module.

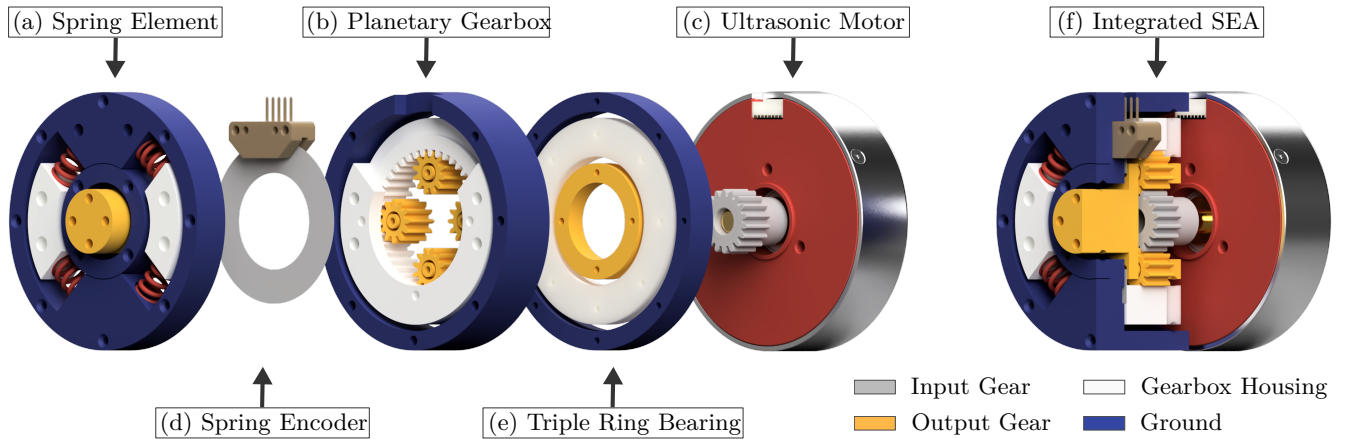


Fig. 3: The architecture of our compact SEA module comprises essential components: a spring element (a), a gearbox (b), an USM (c), and an optical spring encoder (d). Integration is facilitated by a triple ring bearing (e), allowing the entire framework to fit seamlessly into a cylindrical space, as depicted in (f), with a diameter of 80 mm and a total length of 66 mm.

A. Transmission Force Sensing SEA

While a conventional SEA positions its spring element between the output of a geared motor and the load [10], our design follows the same approach as the SEA configuration presented in [16]. In this configuration, the spring element is situated between the gearbox housing and the ground. In this letter, we distinguish the conventional SEA as a direct force sensing series elastic actuator (FSEA) and the variant introduced in [16] as a transmission force sensing series elastic actuator (TFSEA). In Fig. 2, the structural difference between an FSEA and a TFSEA is illustrated. The TFSEA presents several advantages for implementation in MRI scanners. Notably, the spring element is fixed to the ground and motor housing, rather than moving with the actuator output, allowing for compact integration of the motor, gearbox, and spring element. Moreover, placing the electronic components of the spring deflection encoder on the ground side eliminates the need for encoder cable movement. Although gearbox friction and backlash slightly compromise output force sensing accuracy, these drawbacks are outweighed by the benefits.

In Fig. 3 (b), our SEA incorporates a planetary gearbox design. This configuration, akin to the gearbox illustrated in Fig. 2 (b), features a sun gear as the input gear, an assembly of four planet gears serving as the output gear, and an inner ring gear encompassing the planet gears to form the gearbox housing. The gear ratio N_i^o between the input and output is chosen within a range of $\frac{1}{5} \sim \frac{1}{3}$ to avoid excessively small sun or planet gears, which are difficult to manufacture due to material strength limitations. In our prototype, the gear ratio is established at $N_i^o = \frac{3}{10}$.

B. Spring Element

In the realm of rotary SEAs, the adoption of helical torsion springs as elastic elements is well-explored,

as demonstrated in [14], [16]. Specifically, the spring selection in [16] plays a pivotal role in achieving a compact integration of the SEA by encompassing a brushless direct current (BLDC) motor with a helical torsion spring. However, while implementing a helical torsion spring simplifies rotary SEA design, it does not enhance compactness when paired with a disk-shaped USM, which typically has a larger outer diameter and shorter length compared to the BLDC motor used in [16]. To address this, a TFSEA design introduced in [17] employs a customized planar torsion spring element to enhance overall compactness. Nonetheless, this planar torsion spring requires more metals than a helical spring, potentially leading to more interference in MR imaging processes.

Fig. 3 (a) presents the spring element design, drawing inspiration from the SEA in [11]. To address the previously highlighted concerns, the torsion spring element features four off-the-shelf brass helical compression springs arranged in parallel. The loading of these four parallel springs is achieved through two sliders affixed to the housing of the planetary gearbox. Each helical compression spring, with an outer diameter of 9.5 mm and a spring constant of $1.28 \text{ N} \cdot \text{mm}^{-1}$, places its centerline 25 mm from the rotation axis under no additional load.

When torque is applied, the torsion spring element allows for a rotational range of $\pm 12^\circ$, shifting the centerline of each helical compression spring within a range of 24.14 ~ 25.48 mm from the rotation axis of the torsion spring element. Despite this, the total torsion spring rate remains relatively constant, ranging from 3.15 ~ 3.20 $\text{N} \cdot \text{m} \cdot \text{rad}^{-1}$. This consistency is due to the opposing shifts of the centerlines of the two springs on either side of the slider, effectively balancing each other out. At full compression of 12° , the torsion spring element generates maximum torques of 0.67 $\text{N} \cdot \text{m}$ at the gearbox housing and 0.96 $\text{N} \cdot \text{m}$ at the gearbox output.

C. Compact Integration

Fig. 3(f) depicts a half-section view of our compact SEA integration, incorporating the spring element, the planetary gearbox, and a Tekceleo WLG-75-R USM. At the peak SEA output torque of $0.96 \text{ N}\cdot\text{m}$, this USM provides to a maximum velocity of $5.2 \text{ rad}\cdot\text{s}^{-1}$ at the SEA output and yielding a peak output power of 5.0 W .

To assemble the integrated SEA and mitigate off-axis movement of each component with respect to the ground, we have designed a triple-ring ball bearing. As illustrated in Fig. 3(e), this triple-ring bearing secures its inner ring to the output gear, the middle ring to the gearbox housing, and the outer ring to the ground. Within the spring element, an additional ball bearing enforces the constraint between the ground and the output gear. To measure the spring deflection, we employ an US Digital EM2-2-10000-I rotary optical encoder module, with the encoder attached to the grounded housing in the spring element and the codewheel affixed to the gearbox housing. While the majority of the SEA components were fabricated through computer numerical control (CNC) with a tolerance of $\pm 0.1 \text{ mm}$, the gearbox was customized using multi jet fusion (MJF) 3D printing for this prototype. This 3D-printed gearbox introduced backlash, resulting in slight vibrations during operation. As shown in the front view of our SEA in Fig. 5(a), we addressed this issue by adding small foam padding between each spring slider and the ground layer, effectively mitigating gearbox vibrations with minimal additional in-axis friction.

As a whole, the spring element, planetary gearbox, and bearing seamlessly fit within a cylindrical space with an outer diameter of 80 mm and a total length of 39.5 mm . This comprises a 12 mm length for the spring element, 18 mm for the planetary gearbox, and 9.5 mm for the bearing. When combined with a 22.5 mm thick USM and a 4 mm thick aluminum cooling plate for the motor, the integrated SEA has a total length of 66 mm .

In Table I we present a dimensional comparison between our integrated SEA module and other SEAs employing USMs and electromagnetic motors. Our SEA module achieves a power-to-volume density comparable to the linear MRI-compatible SEA described in [12]. Although our SEA module has a lower power-to-volume density than non-MRI-compatible SEAs using electromagnetic motors [15], [16], this is expected due to the inherently lower power density of commercial USMs compared to electromagnetic motors. Additionally, as shown in Table II, the modifications required to enhance MRI compatibility, such as reducing metal usage, have necessitated a larger drivetrain to maintain structural integrity. This trade-off highlights the need to sacrifice some power density to achieve MRI compatibility.

TABLE II: Materials Used in Spring Element, Gearbox, and Bearings

Component	Material	Mass (g)	Volume (cm^3)
Gearbox	Nylon	30.3	30.9
SEA Housing			
Spring Sliders	Acetal	154.8	109.8
Ring Bearings			
Helical Springs			
Heat-Set Inserts	Brass	18.7	2.2
Low-Stress Screws			
High-Stress Screws	SS 316 ¹	7.2	0.9

¹ 316 stainless steel (SS 316) is non-magnetic and acceptable for MRI applications when positioned at a small distance from the region of interest [22].

D. MRI Compatibility

As discussed in [12], the MRI compatibility of an SEA includes the safety and actuator functionality in MRI environment and non-interference in the imaging processes. The safety in MRI environment is ensured by incorporating MRI-safe motor, encoder, and materials into the SEA module. In Sec. IV-A we will show the torque control performance of our SEA in an MRI scanner.

The extent of interference in MR imaging processes is largely contingent on the magnetic susceptibility and conductivity of materials [22]. Similar to the SEA in [12], the spring element, gearbox, and bearings of our SEA module are fabricated from non-magnetic and non-conductive polymers, with only a small volume of metals utilized in the helical compression springs and fasteners, as outlined in Table II. However, the primary source of imaging interference remains the commercial USM. As proposed in [8], [9], USMs should be positioned $20 \sim 30 \text{ cm}$ away from the region of interest for MR imaging. Nonetheless, this distance requirement can be addressed in an integrated design of the robot. The compact nature of our SEA contributes to fulfilling this requirement.

III. MODELING AND CONTROL

In this section, we develop a torque controller for velocity-sourced SEAs, ensuring force regulation in MRI robotic applications with both low and high external impedance, as shown in Fig. 1. To enhance clarity, all variables introduced in our control design are referenced in the output frame of our SEA. First, we define θ_e as the SEA's output displacement. Accordingly, θ_a , θ_s , and k_s denote the reflected USM's displacement, spring deflection, and spring stiffness respectively, transitioning from their original reference frames to the output frame. The output torque τ_s exerted by the spring in our SEA

TABLE I: Comparison to Other SEAs for MRI and Non-MRI Applications

Reference	MRI	SEA Type	Motor	Drivetrain Dimensions ¹	Motor Dimensions ¹	Enclosed Volume ²	Peak Power ³	Power Density
				W × H × D (cm)	W × H × D (cm)	(cm ³)	(W)	(W · cm ⁻³)
Ref. [12]	Yes	Linear	USM	6.7 × 6.7 × 17.6	6.7 × 7.7 × 6.6	1130.6	2.2	1.95 × 10 ⁻³
Ref. [15]	No	Linear	BLDC	5.2 × 5.2 × 14.0	3.0 × 3.0 × 10.0	468.6	110.0	2.35 × 10 ⁻¹
Ref. [16]	No	Rotary	BLDC	6.0 × 6.0 × 17.2		619.2	681.5	1.10 × 10 ⁰
This Paper	Yes	Rotary	USM	8.0 × 8.0 × 6.6		422.4	5.0	1.18 × 10 ⁻²

¹ The exact dimensions for the SEAs in [12], [15], [16] are not provided. The listed dimensions are approximations based on [12, Fig. 2], [15, Fig. 3], [16, Fig. 7] with reference to their motor dimensions. ² The enclosed volume of an SEA is defined as the total volume of the listed rectangular regions for its drivetrain and motor. ³ The peak output power for the SEAs in [12], [15] are calculated based on their applications in [20], [21].

is computed from the spring encoder measurements of θ_s using Hooke's law: $\tau_s = k_s \cdot \theta_s$. The output displacement θ_e , is computed as the difference between the USM's encoder measurements of θ_a and the spring encoder measurements of θ_s . In addition, we define ω_e , ω_a , and ω_s as the time derivative of θ_e , θ_a , and θ_s .

A. Modeling

In Fig. 4(a), we model the external system dynamics that attach to the output of our SEA as a mass m_e , a damper b_e , and an external force source τ_e . Let $Z_s(s)$ and $Z_e(s)$ be the impedance models for the actuator spring and the external system, respectively. According to the equations of motion with θ_a and θ_e , we define $Z_s(s)$ and $Z_e(s)$ as

$$Z_s(s) \triangleq \frac{\tau_s}{\omega_s} = \frac{\tau_s}{\omega_a - \omega_e} = k_s s^{-1}, \quad (1)$$

$$Z_e(s) \triangleq \frac{\tau_s - \tau_e}{\omega_e} = m_e s + b_e. \quad (2)$$

Combining (1) and (2), we eliminate ω_e in the expression and derive an expression for τ_s in terms of the motor velocity input ω_a and the external force input τ_e :

$$\tau_s = G_{sa}(s) \cdot \omega_a + G_{se}(s) \cdot \tau_e, \quad (3)$$

with the transfer functions $G_{sa}(s)$ and $G_{se}(s)$ define as

$$G_{sa}(s) \triangleq \frac{Z_s Z_e}{Z_s + Z_e} = \frac{k_s(m_e s + b_e)}{m_e s^2 + b_e s + k_s}, \quad (4)$$

$$G_{se}(s) \triangleq \frac{Z_s}{Z_s + Z_e} = \frac{k_s}{m_e s^2 + b_e s + k_s}. \quad (5)$$

By including a velocity-controlled USM transfer function $G_a(s) \triangleq \frac{\omega_a}{\omega_a^d}$ with a 50 Hz bandwidth, we obtain

$$\tau_s = G_{sa}^d(s) \cdot \omega_a^d + G_{se}(s) \cdot \tau_e, \quad (6)$$

where ω_a^d is the desired motor velocity and $G_{sa}^d(s) \triangleq G_{sa}(s)G_a(s)$. As indicated in Sec. II-C, ω_a^d is set within $\pm 5.2 \text{ rad} \cdot \text{s}^{-1}$ due to the velocity limits of the USM.

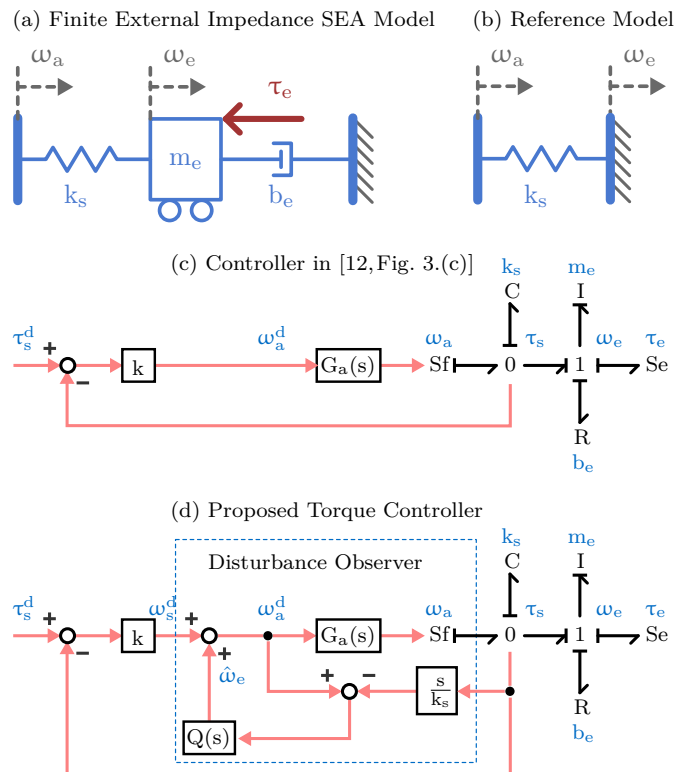


Fig. 4: In (a), the velocity-sourced SEA encounters uncertain and finite external impedance, posing challenges to force control. Conversely, our DOB's reference model in (b) has an infinitely large external impedance attached to its output. Unlike the direct force controller depicted in (c), as proposed in [12, Fig. 3.(c)], our control framework in (d) incorporates the DOB to compel the actual velocity-sourced SEA system to emulate the behavior of the reference model. This framework ensures that a proportional controller can achieve effective force reference tracking despite the uncertain external impedance. The bond graphs in (c) and (d) represent the SEA model in (a). In the bond graphs, I, R, C, Sf, and Se denote the nodes representing inertia, damper, spring, velocity source, and force source, respectively, in a mechanical system.

B. DOB-Based Torque Control

In Fig. 1 we illustrate how the SEA force controller must manage both minimal external impedance before patient contact and significant impedance upon contact. According to [3], the SEA force controller is more effective with larger external impedance, resulting in a higher gain G_{sa} for the motor input ω_a and a lower gain G_{se} for the disturbance force τ_e . Particularly, as $Z_e \rightarrow \infty$ in [4] and [5], we have $G_{sa} \rightarrow Z_s$ and $G_{se} \rightarrow 0$, leading to our DOB's reference model shown in Fig. 4(b). This reference model $G_{sa}(s) = Z_s(s)$, an integrator multiplied by actuator spring constant k_s , enables stabilization with a single proportional controller $\omega_a^d = k \cdot (\tau_s^d - \tau_s)$ for effective force reference tracking.

In Fig. 4(d), we show the proposed DOB for imposing the reference model without actually having $Z_e = \infty$. Under this DOB, we estimate the output velocity ω_e as

$$\hat{\omega}_e = Q(s) \cdot (\omega_a^d - Z_s^{-1} \cdot \tau_s) \quad (7)$$

where $Q(s)$ is a low-pass filter of sufficient order to ensure the observer is causal. By implementing

$$\omega_a^d = \omega_s^d + \hat{\omega}_e, \quad (8)$$

we have the desired velocity ω_s^d for spring deflection as the new control input of the actuator system. Substituting [7] and [8] into [3], we obtain

$$\tau_s = G_{ss}^d(s) \cdot \omega_s^d + \hat{G}_{se}(s) \cdot \tau_e. \quad (9)$$

where

$$G_{ss}^d(s) \triangleq \frac{Z_s Z_e G_a}{Q Z_e G_a + (1-Q)(Z_s + Z_e)}, \quad (10)$$

$$\hat{G}_{se}(s) \triangleq \frac{(1-Q)Z_s}{Q Z_e G_a + (1-Q)(Z_s + Z_e)}. \quad (11)$$

Particularly, as $Q \rightarrow 1$ in [10] and [11], we have $G_{ss}^d \rightarrow Z_s$ and $\hat{G}_{se} \rightarrow 0$, thereby imposing the reference model in Fig. 4(b).

C. Comparison to Direct P and PI Control

If we incorporate a first-order filter $Q(s) = \frac{\alpha}{s+\alpha}$ into the proposed spring force controller in Sec. III-B, equations [10] and [11] can be expressed as follows:

$$G_{ss}^d(s) = \frac{Z_s Z_e G_a}{Z_s + Z_e + Z_e G_a \cdot \alpha \cdot s^{-1}} \cdot \frac{s + \alpha}{s}, \quad (12)$$

$$\hat{G}_{se}(s) = \frac{Z_s}{Z_s + Z_e + Z_e G_a \cdot \alpha \cdot s^{-1}}. \quad (13)$$

By having a small value for the pole α , we can neglect the term $Z_e G_a \cdot \alpha \cdot s^{-1}$ in the denominators of [12] and

[13]. Consequently, we obtain the approximations:

$$G_{ss}^d(s) \approx G_{sa}^d(s) \cdot \frac{s + \alpha}{s}, \quad \text{for small } \alpha, \quad (14)$$

$$\hat{G}_{se}(s) \approx G_{se}(s), \quad \text{for small } \alpha. \quad (15)$$

Notice that the term $\frac{s+\alpha}{s}$ in [14], combined with the proportional gain k outside of the disturbance observer (DOB) loop, constitutes a PI compensator $k \cdot \frac{s+\alpha}{s}$, which is similar to the force controller in [13]. However, in contrast to the direct P and PI control methods in [11], [12], [13], our proposed control approach based on DOB yields several advantages.

As the pole value α increases from 0 in [12], the term $\frac{s+\alpha}{s}$ plays a crucial role in mitigating steady-state errors in the closed loop, presenting an improvement over a direct P controller in [12]. Moreover, with a continued increase in α , the influence of the term $Z_e G_a \cdot \alpha \cdot s^{-1}$ in the denominators of [12] and [13] becomes more pronounced. This term, $Z_e G_a \cdot \alpha \cdot s^{-1}$, drives $G_{ss}^d \rightarrow Z_s$ and $\hat{G}_{se} \rightarrow 0$, enhancing reference tracking performance and reducing sensitivity to external input τ_e in the closed loop. These enhancements go beyond the capabilities of a direct PI controller.

D. Controller Parameter Tuning

In Sec. III-C, we demonstrate that $G_{ss}^d \rightarrow Z_s$ and $\hat{G}_{se} \rightarrow 0$ as $\alpha \rightarrow \infty$. Since $Z_s = \frac{k_s}{s}$ is the spring stiffness k_s multiplied by an integrator $\frac{1}{s}$, it is straightforward to tune a proportional controller $\omega_a^d = k \cdot (\tau_s^d - \tau_s)$ for the closed-loop force control of our SEA.

However, an infinitely high value of α is impractical for several reasons. As $\alpha \rightarrow \infty$, $Q(s) \rightarrow 1$, causing the inverse model $Z_s^{-1} = \frac{s}{k_s}$ in [7] not realizable in a digital system and increasing sensitivity to sensor noise from the spring deflection encoder. To mitigate sensitivity to sensor noise while using higher values of α , we employ $Q(s)$ as a second-order Butterworth filter $Q(s) = \frac{\alpha^2}{s^2 + 2\zeta\alpha s + \alpha^2}$, where $\zeta = \frac{\sqrt{2}}{2}$ ensures that $Q(s)$ has its cutoff frequency at α .

Moreover, the 50 Hz bandwidth of the motor velocity controller in $G_a(s)$ imposes constraints on the values of both the $Q(s)$ filter cutoff frequency α and the proportional gain k . Adhering to this bandwidth limitation, the DOB-based controller is configured with $k = \frac{60}{k_s}$ and $\alpha = 120 \text{ rad} \cdot \text{s}^{-1}$ ($\approx 19.1 \text{ Hz}$) throughout our experiments. This controller configuration is designed to provide a bandwidth of $60 \text{ rad} \cdot \text{s}^{-1}$ ($\approx 9.5 \text{ Hz}$) and a time constant of $t_c = \frac{1}{60}$ sec for the closed-loop force control of our SEA.

IV. EXPERIMENTAL VALIDATION AND BENCHMARKING

In Table III we summarize the hardware and controller configurations utilized throughout the experiments T-A-M, T-A-1, T-A-2, T-B-1, and T-B-2 presented in this section. T-A-M, T-A-1, and T-A-2 correspond to the low impedance tests in Sec. IV-A, while T-B-1 and

T-B-2 correspond to the high impedance tests in Sec. IV-B. We experimentally validate the SEA’s capability to track force references within and outside the MRI environment. Following this assessment, perturbation tests on the SEA are conducted. For each experimental category, we present a performance evaluation comparing our DOB-based force controller with the direct force controller in [12].

Fig. 5 shows the hardware setup for the experimental validation of the compact SEA. The SEA is governed by a microcontroller unit (MCU), which acquires motor position θ_a and spring deflection θ_s measurements from encoders. Based on these measurements, the MCU sends motor velocity command ω_a^d to the USM driver at 1000 Hz.

A. MRI and Non-MRI Pendulum Tests

In T-A-M, T-A-1, and T-A-2, we connect the output gear of our SEA to a pendulum rod constructed from acrylonitrile butadiene styrene (ABS) via 3D printing. As depicted in Fig. 5(d), this pendulum rod supports a 125 g brass load positioned 12 cm from its center of rotation. This setup results in a moment of inertia of $m_e = 1.8 \times 10^{-3} \text{ kg} \cdot \text{m}^2$, representing a low external impedance to our SEA.

In T-A-M, this setup is positioned to the center of the bore in a GE MR750W scanner, a 3T MRI machine as depicted in Fig. 5(c). In T-A-1 and T-A-2, we move this setup to a non-MRI environment. Moreover, in T-A-2, we incorporate a direct P controller with an identical proportional gain $k = \frac{60}{k_s}$ for comparison with the proposed DOB-based controller employed in T-A-M and T-A-1.

The angular position θ_e of the pendulum rod follows a 0.5 Hz triangle wave reference signal $\theta_e^d(t)$ through an impedance controller

$$\tau_s^d = k_v \cdot (\theta_e^d - \theta_e) + b_v \cdot (\omega_e^d - \dot{\omega}_e), \quad (16)$$

where k_v is a virtual spring stiffness, b_v is a virtual damper coefficient, ω_e^d is the derivative of θ_e^d , and $\dot{\omega}_e$ is the output velocity estimate introduced in (7). We set $k_v = 0.5 \cdot k_s$ and $b_v = 0.02 \cdot k_s$, allowing the SEA to respond to the external force and dynamics with a stiffness reduced to half of its original value k_s .

In Fig. 6(a)-(b), we present the experimental results from T-A-M and T-A-1, showing the reference tracking performance of our SEA pendulum system in both MRI and non-MRI environments. These results reveal equivalent responses in the output torque tracking error $\tau_s - \tau_s^d$ for both T-A-M and T-A-1, including the steady-state responses and transient responses to the commands of τ_s^d . Notably, both experiments exhibit a settling time of the transient response around 0.1 sec, which is six times the time constant $t_c = \frac{1}{60}$ sec of the desired closed-loop SEA transfer function, and maintain a steady-state error within $\pm 0.02 \text{ N} \cdot \text{m}$, which is 2% of the maximum output torque. The consistent time response of θ_e and

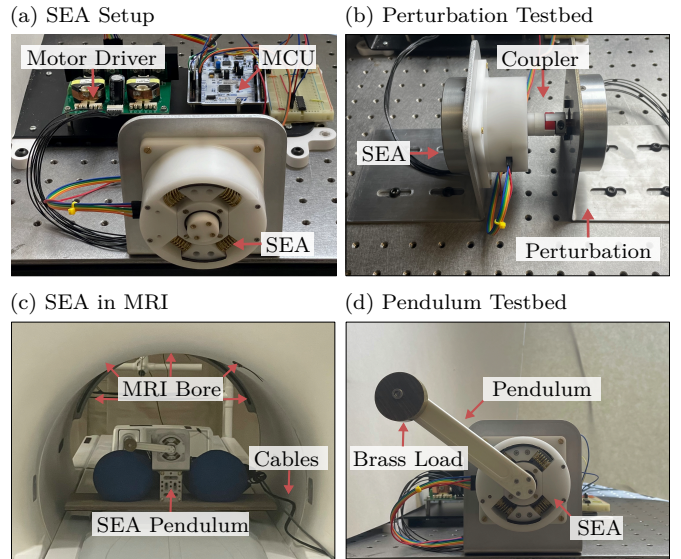


Fig. 5: In our experimental setup, the SEA is controlled by a NUCLEO-F446RE MCU in (a), which gathers position measurements from encoders and sends motor velocity commands to the USM driver. The perturbation testbed in (b) consists of our SEA module on the left and an additional USM on the right, serving as the perturbation source. The outputs of these two actuators are connected through a shaft coupler. In our MRI test setup depicted in (c), a SEA pendulum testbed in (d) is positioned at the center of the bore of a 3T MRI scanner. The motor driver and MCU are located outside the MRI room, transmitting power and control signals through 10-meter-long cables, as illustrated in (c).

TABLE III: Experimental Setting

Index	In MRI	Testbed	External Impedance	Torque Control
T-A-M	Yes	Pendulum	Low Impedance	DOB-Based
T-A-1	No	Pendulum	Low Impedance	DOB-Based
T-A-2	No	Pendulum	Low Impedance	Direct P in [12]
T-B-1	No	Perturbation	High Impedance	DOB-Based
T-B-2	No	Perturbation	High Impedance	Direct P in [12]

τ_s across T-A-M and T-A-1 demonstrate that our SEA is not affected by the 3-T magnetic field, indicating its suitability for MRI applications.

In contrast to the satisfactory torque tracking performance exhibited in T-A-M and T-A-1, the implementation of a direct P controller in T-A-2 yields a steady-state torque error of approximately $0.33 \text{ N} \cdot \text{m}$, 34% of the maximum output torque, as illustrated in Fig. 6(c).

B. Perturbation Tests

In Fig. 5(b), the output gear of the SEA is mechanically linked via a shaft coupler to the output shaft of an additional USM, which serves as the source of external perturbation. This supplementary motor introduces per-

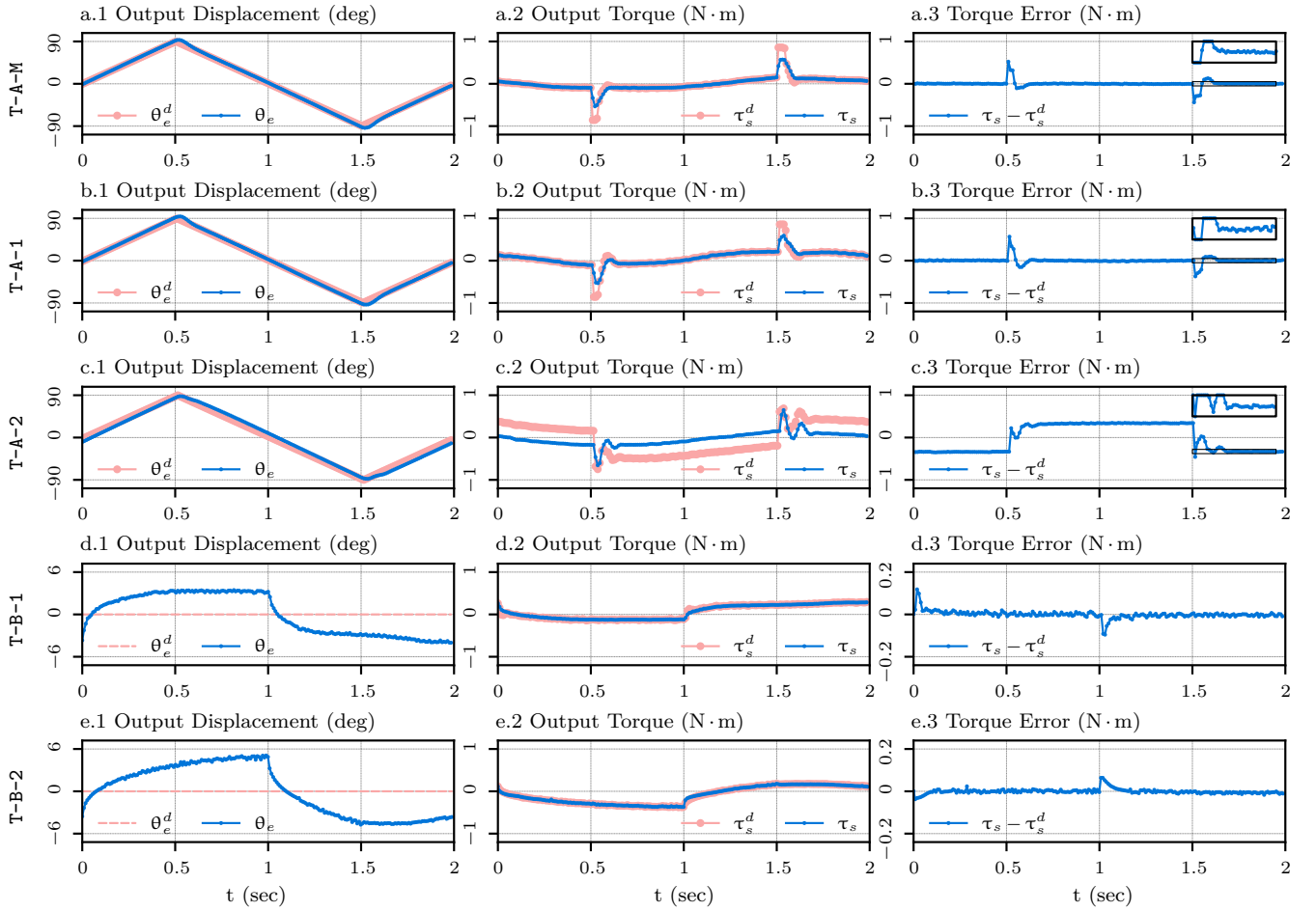


Fig. 6: Experimental results from T-A-M, T-A-1, T-A-2, T-B-1, and T-B-2 are presented in distinct rows. The first column corresponds to the SEA output displacement θ_e , the second column represents the SEA output torque τ_s , and the third column displays the torque tracking error $\tau_s - \tau_s^d$. In a.3, b.3, and c.3, small windows are zoomed into the highlighted impulse response details of $\tau_s - \tau_s^d$. These small windows share the same scale as d.3 and e.3.

turbation by tracking a small-magnitude triangle wave reference signal from its control side. Notably, due to the significantly higher impedance of the USM compared to the SEA spring element, the perturbation motor effectively acts as a velocity source, contributing to the disturbance variable ω_e .

In T-B-1 and T-B-2, we assess the effectiveness of our DOB-based controller alongside the same direct P controller as T-A-2 using the high-impedance perturbation test setup. Similar to the pendulum tests, we implement an impedance controller defined in (16) with $k_v = 0.5 \cdot k_s$ and $b_v = 0.02 \cdot k_s$. The reference θ_e^d in (16) is set to zero, attempting to keep the SEA stationary in response to external perturbations.

Fig. 6.(d)-(e) depict the experimental results from T-B-1 and T-B-2. The torque error $\tau_s - \tau_s^d$ in T-B-1 resembles the outcomes observed in T-A-M and T-A-1, except for the peak values in the transient responses, which are mitigated by a slight compliance from the shaft coupler used in the perturbation testbed. In comparison to the results obtained in T-A-2, the direct P controller in T-B-2 eradicates the steady-state torque bias.

C. Benchmarking Analysis

Assuming $G_a(s) \approx 1$ at low frequencies, the closed-loop transfer function for the direct P control method in [12] is $G_{CL}^P(s) = \frac{k \cdot G_{sa}(s)}{1 + k \cdot G_{sa}(s)}$, where $G_{sa}(s)$ is defined in (4). When $Z_e(s)$ is small, it simplifies to $G_{CL}^P(s) \approx \frac{k \cdot Z_e(s)}{1 + k \cdot Z_e(s)}$, resulting in a closed-loop gain significantly below 1. In the outcomes of T-A-2, the direct P controller exhibits inadequate steady-state performance under low external impedance scenarios. When $Z_e(s)$ is large, $G_{sa}(s) \approx Z_s(s) = \frac{k_s}{s}$, resulting in a closed-loop gain $G_{CL}^P(s) \approx 1$ in the steady state. Consequently, the performance improves considerably under high external impedance conditions, as demonstrated in T-B-2. However, transitioning from low to high impedance scenarios, as depicted in Fig. 1, may necessitate a large actuator force to eliminate the steady-state torque error.

In [11], [13], velocity-sourced SEAs incorporate a PI compensator to mitigate steady-state tracking errors. In contrast to the 1st-order PI controller employed in [13], the SEA system presented in [11] utilizes a 2nd-order PI controller by cascading two 1st-order PI controllers.

The design of this 2nd-order PI controller strategically positions its two zeros to cancel the resonant poles of $G_{sa}(s)$ in (4). However, without prior knowledge of $Z_e(s)$, both the 1st-order and 2nd-order PI compensators may introduce stability issues to the closed-loop SEA system.

In our proposed force controller, we employ a DOB to compel the SEA to emulate the reference model represented by $\frac{k_s}{s}$ in the presence of varying external impedance. The integrator in the reference model naturally mitigates steady-state errors. In the comparison between T-A-1 and T-B-1, we showcase the robustness of our DOB-based force controller with both low and high external impedance.

V. CONCLUSION

In this letter, we present a compact, efficient rotary SEA module compatible with MRI environments, driven by velocity-sourced ultrasonic motors. Using a DOB-based controller, we achieve robust torque control for both low and high impedance loads. Tests in a 3 Tesla MRI scanner confirm the SEA's effectiveness, with a quick response time (0.1 seconds) and minimal torque error (within 2% of peak). Future work will aim to improve performance and explore clinical applications.

ACKNOWLEDGEMENT

We thank Alfredo De Goyeneche and Dr. Michael Lustig for their valuable assistance during the MRI test.

REFERENCES

- [1] H. Su, K.-W. Kwok, K. Cleary, I. Iordachita, M. C. Cavusoglu, J. P. Desai, and G. S. Fischer, "State of the art and future opportunities in MRI-guided robot-assisted surgery and interventions," *Proceedings of the IEEE*, vol. 110, no. 7, pp. 968–992, 2022.
- [2] Z. Guo, Z. Dong, K.-H. Lee, C. L. Cheung, H.-C. Fu, J. D. Ho, H. He, W.-S. Poon, D. T.-M. Chan, and K.-W. Kwok, "Compact design of a hydraulic driving robot for intraoperative MRI-guided bilateral stereotactic neurosurgery," *IEEE Robotics and Automation Letters*, vol. 3, no. 3, pp. 2515–2522, 2018.
- [3] Z. Dong, Z. Guo, K.-H. Lee, G. Fang, W. L. Tang, H.-C. Chang, D. T. M. Chan, and K.-W. Kwok, "High-performance continuous hydraulic motor for MR safe robotic teleoperation," *IEEE Robotics and Automation Letters*, vol. 4, no. 2, pp. 1964–1971, 2019.
- [4] N. Yu, C. Hollnagel, A. Blickenstorfer, S. S. Kollias, and R. Riener, "Comparison of MRI-compatible mechatronic systems with hydrodynamic and pneumatic actuation," *IEEE/ASME Transactions on Mechatronics*, vol. 13, no. 3, pp. 268–277, 2008.
- [5] R. Monfaredi, K. Cleary, and K. Sharma, "MRI robots for needle-based interventions: systems and technology," *Annals of biomedical engineering*, vol. 46, pp. 1479–1497, 2018.
- [6] R. Gassert, R. Moser, E. Burdet, and H. Bleuler, "MRI/fMRI-compatible robotic system with force feedback for interaction with human motion," *IEEE/ASME Transactions on Mechatronics*, vol. 11, no. 2, pp. 216–224, 2006.
- [7] A. Yamamoto, K. Ichiyonagi, T. Higuchi, H. Imamizu, R. Gassert, M. Ingold, L. Sache, and H. Bleuler, "Evaluation of mr-compatibility of electrostatic linear motor," in *2005 IEEE International Conference on Robotics and Automation*, 2005, pp. 3658–3663.
- [8] G. S. Fischer, A. Krieger, I. Iordachita, C. Csoma, L. L. Whitcomb, and G. Fichtinger, "MRI compatibility of robot actuation techniques—a comparative study," in *2008 International Conference on Medical Image Computing and Computer-Assisted Intervention*. Springer, 2008, pp. 509–517.
- [9] A. Krieger, S.-E. Song, N. B. Cho, I. I. Iordachita, P. Guion, G. Fichtinger, and L. L. Whitcomb, "Development and evaluation of an actuated MRI-compatible robotic system for MRI-guided prostate intervention," *IEEE/ASME Transactions on Mechatronics*, vol. 18, no. 1, pp. 273–284, 2011.
- [10] G. A. Pratt and M. M. Williamson, "Series elastic actuators," in *Proceedings 1995 IEEE/RSJ International Conference on Intelligent Robots and Systems. Human Robot Interaction and Cooperative Robots*, vol. 1, 1995, pp. 399–406.
- [11] G. Wyeth, "Demonstrating the safety and performance of a velocity sourced series elastic actuator," in *2008 IEEE International Conference on Robotics and Automation*, 2008, pp. 3642–3647.
- [12] F. Sergi, A. C. Erwin, and M. K. O'Malley, "Interaction control capabilities of an MR-compatible compliant actuator for wrist sensorimotor protocols during fMRI," *IEEE/ASME Transactions on Mechatronics*, vol. 20, no. 6, pp. 2678–2690, 2015.
- [13] Y. M. Senturk and V. Patoglu, "MRI-VisAct: a Bowden-cable-driven MRI-compatible series viscoelastic actuator," *Transactions of the Institute of Measurement and Control*, vol. 40, no. 8, pp. 2440–2453, 2018.
- [14] K. Kong, J. Bae, and M. Tomizuka, "A compact rotary series elastic actuator for human assistive systems," *IEEE/ASME Transactions on Mechatronics*, vol. 17, no. 2, pp. 288–297, 2011.
- [15] N. Paine, S. Oh, and L. Sentis, "Design and control considerations for high-performance series elastic actuators," *IEEE/ASME Transactions on Mechatronics*, vol. 19, no. 3, pp. 1080–1091, 2013.
- [16] C. Lee and S. Oh, "Configuration and performance analysis of a compact planetary geared elastic actuator," in *IECON 2016-42nd Annual Conference of the IEEE Industrial Electronics Society*, 2016, pp. 6391–6396.
- [17] T. Kim, K. Shi, and K. Kong, "A compact transmitted-force-sensing series elastic actuator with optimized planar torsional spring for exoskeletons," in *2021 IEEE/ASME International Conference on Advanced Intelligent Mechatronics (AIM)*, 2021, pp. 572–577.
- [18] W.-H. Chen, J. Yang, L. Guo, and S. Li, "Disturbance-observer-based control and related methods—an overview," *IEEE Transactions on Industrial Electronics*, vol. 63, no. 2, pp. 1083–1095, 2015.
- [19] T. Nakamura, D. Yashiro, K. Yubai, and S. Komada, "Torque control of a series elastic actuator using an ultrasonic motor with angular-velocity saturation," *Electrical Engineering in Japan*, vol. 214, no. 2, p. e23297, 2021.
- [20] A. Erwin, M. K. O'Malley, D. R. Rens, and F. Sergi, "Development, control, and MRI-compatibility of the MR-softwrist," in *2015 IEEE International Conference on Rehabilitation Robotics (ICORR)*, 2015, pp. 187–192.
- [21] J. Kwak, W. Choi, C. Lee, and S. Oh, "Gravity and impedance compensation of body weight support system driven by two series elastic actuators," *IEEE/ASME Transactions on Mechatronics*, vol. 27, no. 1, pp. 190–201, 2021.
- [22] H. Elhawary, Z. T. H. Tse, A. Hamed, M. Rea, B. L. Davies, and M. U. Lamperth, "The case for MR-compatible robotics: a review of the state of the art," *The International Journal of Medical Robotics and Computer Assisted Surgery*, vol. 4, no. 2, pp. 105–113, 2008.